




# Different electrodeposition techniques of manganese and nickel oxide on nickel foam and their effect on improved supercapacitor behaviour: a comparative study

Asha Raveendran<sup>1</sup>, Mijun Chandran<sup>2</sup>, Masoom Raza Siddiqui<sup>3</sup>, Saikh Mohammad Wabaidur<sup>3</sup>, Muthusankar Eswaran<sup>4</sup>, and Ragupathy Dhanusuraman<sup>1,5,\*</sup> 

<sup>1</sup> Nano Electrochemistry Lab (NEL), Department of Chemistry, National Institute of Technology Puducherry, Karaikal 609609, India

<sup>2</sup> Department of Chemistry, Central University of Tamil Nadu, Thiruvarur 610005, India

<sup>3</sup> Chemistry Department, College of Science, King Saud University, Riyadh 11451, Saudi Arabia

<sup>4</sup> Division of Systems and Synthetic Biology, Department of Biology and Biological Engineering, Chalmers University of Technology, 41296 Göteborg, Sweden

<sup>5</sup> Nano Electrochemistry Laboratory (NEL), Central Instrumentation Facility (CIF), Pondicherry University, Puducherry 605014, India

**Received:** 20 June 2023

**Accepted:** 2 October 2023

**Published online:**  
24 October 2023

© The Author(s), under exclusive licence to Springer Science+Business Media, LLC, part of Springer Nature, 2023

## ABSTRACT

Manganese and Nickel oxides were electrodeposited onto Nickel foam by potentiodynamic (10, 25 and 50 cycles), potentiostatic and galvanostatic modes and the effects of different electrodeposition techniques on the elemental compositions and their supercapacitive behaviour were studied to optimise the most appropriate electrodeposition technique for supercapacitor application. The structural properties, morphology and elemental analysis were studied by X-ray Diffraction (XRD), Scanning Electron Microscopy (SEM) accompanied by Energy-Dispersive X-Ray Analysis (EDX). The electrodes' functional groups were analysed via Fourier Transform-Infrared Spectroscopy (FT-IR). Their electrochemical supercapacitive performance were assessed by calculating the areal capacitance from cyclic voltammograms (CV), from Galvanostatic charge-discharge Curves (GCD), and their behaviour was accessed by Electrochemical impedance spectroscopy (EIS) analyses in 0.1 M KOH. The electrochemical results specified among the different electrode MN10, MN25, MN50 (potentiodynamic electrodeposition), MNCA (electrodeposition via chronoamperometry) and MNCP (electrodeposition via chronopotentiometry); MN25 delivered the highest areal capacitance areal capacitance 256.08 F cm<sup>-2</sup>, with energy density 12.81 Wh cm<sup>-2</sup> and power density 150.71 W cm<sup>-2</sup> with the capacitance retention percentage of 80.5% at 5 Acm<sup>-2</sup> after 5000 cycles.

Address correspondence to E-mail: ragu@pondiuni.ac.in; ragu.nitpy@gmail.com

## 1 Introduction

The start of the twenty-first century witnessed the hike in fossil fuel consumption due to the rapidly rising global economy leading to serious environmental issues like pollution and global warming. These critical issues necessitate the urgent need for alternative energy sources and storage and energy conversion, green, sustainable, yet efficient [1–5]. Among them, Supercapacitors, i.e. electrochemical energy storage (EES) devices, are the most sought after and were first introduced in the 1970s by NCE to provide backup power for computers [6–8]. Over the years, researchers have manufactured modified supercapacitors to play a crucial role in applications such as portable electronic devices, especially in the mobile technology and also to enhance the battery or fuel cell system in hybrid electric vehicles owing to their characteristic properties such as excellent power density compared to batteries, fast charging and discharging rate and long cyclic stability. EES comprises two electrodes divided by a separator immersed in an electrolyte. Thus, research is going on to develop highly effective yet low cost, environment-friendly electrode materials as they play a vital role in achieving super capacitive properties [9–12]. Attributing to large specific surface area, apt pore size & their physicochemical properties; transition metal oxides with various valence states such as MnO, RuO, NiO etc. are intriguing materials for supercapacitor electrodes having pseudocapacitive behaviour [13–15]. Transition metal oxides as active electrode materials with varying morphologies are synthesised by chemical as well electrochemical methods. Chemical methods techniques like sputtering, impregnations etc. are multistep processes which give uncontrolled structures and require high temperatures and also have impurities in the synthesised materials [16]. For large scale applications, electrodeposition has been considered as they are economical, can be prepared via simple and low-temperature processing with controlled and uniformly dispersed morphology by varying the electrochemical parameters [17, 18]. The different electrodeposition techniques for the synthesis of electrocatalysts are potentiodynamic electrodeposition, potentiostatic electrodeposition as well as galvanostatic electrodeposition. The current is kept constant in galvanostatic electrodeposition, in potentiostatic electrodeposition method; the potential is applied for a certain time and in

potentiodynamic electrodeposition; the potential of is varied at a particular rate by applying current [19].

Ruthenium oxide as supercapacitor material is considered because of their significantly higher specific capacitance, however due to their high cost; alternatives are sought after [20]. Manganese dioxide ( $\text{MnO}_2$ ), first reported by Lee and Goodenough in 1999; owing to their simple preparation process, low toxicity, good electrochemical activity as well being cost effective have gained tremendous attention from researchers worldwide as potential supercapacitor material [20–24]. Their further development was however limited due to poor ion diffusion constant, low conductivity and weak stability [25, 26]. In order to enhance the electrochemical properties,  $\text{MnO}_2$  accompanied by other metal oxides can be uniformly modifies onto porous electrodes such as carbon material, Ni foam [27]. Such porous electrodes act as stable current collector and are highly conductive due to ion diffusion through their porous structure [28–31]. Metal oxide-based supercapacitors utilize Potassium hydroxide as common alkaline electrolyte, while sulphuric acid is the common acid electrolyte among aqueous electrolytes owing to their ionic conductivity leading to increased power density and reduced internal resistance. This is due to involvement of hydroxide ions and hydrogen ion in proton transport/hopping. However acid electrolytes lead to corrosion and thus is not commonly used. Among other alkaline electrolytes like NaOH and LiOH, KOH, the  $\text{K}^+$  ion exhibits the highest ionic conductivity  $73.5 \text{ Scm}^2\text{mol}^{-1}$  while  $\text{Na}^+$  has  $50.11 \text{ Scm}^2\text{mol}^{-1}$  and  $\text{Li}^+$  has  $38.69 \text{ Scm}^2\text{mol}^{-1}$  respectively [32–34]. In aqueous solution,  $\text{Li}^+$  ion showcases the highest hydrated radius which leads to restricted mobility and hence lowering faradaic current compared to  $\text{K}^+$  and  $\text{Na}^+$ . Though high concentration of KOH can lead to larger peak area and broader cyclic voltammograms which indicates improved capacitive performance; the downfall of higher concentration is corrosion of the working electrode as well as current collector which deteriorates the devices overall performance. Hence for this work the authors have chosen 1 M KOH to do the supercapacitive studies.

The aim of the present investigation is the electrodeposition of manganese and nickel oxide on nickel foam using potentiostatic, potentiodynamic and galvanostatic modes. Nickel oxides is considered since they enhance electrochemical properties by the converting Ni to Ni (II), having many oxidation states, validating more faradaic processes leading increased

psuedocapacitance [35–37]. The nickel foam which is macroporous assist as conductive pathway as well as backbone for both Manganese and nickel oxides. The effects of the three electrodeposition techniques on morphological, structural as well as supercapacitive properties of the fabricated composite on nickel foam have been investigated in this work.

## 2 Experimental section

### 2.1 Materials

Manganese acetate tetrahydrate [ $\geq 99.9\%$ ], Nickel sulphate hexahydrate [ACS reagent,  $\geq 98\%$ ], Potassium hydroxide [ACS reagent,  $\geq 85\%$ , pellets], sulphuric acid (reagent grade) were procured from Merck India. Milli-Q water was used to make the aqueous solutions. Nickel foam was used for the electrodeposition with dimension of 2.5 cm height, 1 cm width, and 1 mm thickness.

### 2.2 Instrumentations

The morphology was examined using scanning electron microscopy (SEM) images along with the elemental distribution of the modified electrodes were done using JCM-7000 NeoScope Benchtop. X-ray diffraction (XRD) analysis was carried out with PANalytical X'Pert PRO equipped with an X'Celerator position sensitive detector with Cu K radiation of wavelength =  $1.5401 \text{ \AA}$ , where the crystalline structure of manufactured electrodes was examined. ATR-FTIR spectroscopy was used to investigate the functional groups of the electrodes in the wave region between  $4000$  and  $400 \text{ cm}^{-1}$  using the ATR-FTIR Spectrometer PerkinElmer Spectrum two. The electrochemical performance of electrodeposited electrodes were tested utilising the OrigaLys-OFG500 electrochemical work station.

### 2.3 Electrochemical measurements

Electrochemical deposition and supercapacitive studies were carried out using the OrigaLys-OFG500 electrochemical work station with three electrode setup. Nickel foam is used as the working electrode, Ag/AgCl is used as the reference electrode, and platinum wire is used as the counter electrode in this configuration. Nickel foams were utilised as current collectors, and

they were cleaned for 5 min in an ultrasonic bath with acetone and deionized water. They were then sonicated for 10 min in a 4 M HCl solution, rinsed with distilled water and 100% ethanol, then dried for 2 h in a vacuum oven at  $60 \text{ }^\circ\text{C}$  [38]. Manganese and Nickel on Nickel Foam electrodes electrodeposited via different cycles of cyclic voltammetry, chronoamperometry and chronopotentiometry in 0.1 M KOH and were studied for their supercapacitive behaviour, charge transfer resistance and stability.

### 2.4 Electrodeposition manganese and nickel on nickel foam

The cleaned Nickel foam was placed in 0.1 M of  $((\text{CH}_3\text{COO})_2 \text{Mn} \cdot 4\text{H}_2\text{O})$  in 0.1 M of  $\text{Na}_2\text{SO}_4$  in 100 mL of deionised water and was electrodeposited via cyclic voltammogram at scan rate of  $10 \text{ mVs}^{-1}$  in the voltage window 0 to 1.2 V; for chronoamperometry, a constant voltage of 1.2 V was applied and; for chronopotentiometry, a constant current at 8mA was maintained for 10 min. For the deposition of Nickel, the Manganese deposited electrode was immersed in 0.2 M  $\text{NiSO}_4$  in 0.1 M  $\text{H}_2\text{SO}_4$  and chronoamperometry, chronopotentiometry and cyclic voltammetry were carried out in the potential window of 0 to 0.6 V.

## 3 Results and discussion

### 3.1 Structural studies

The structural analysis of electrodeposited Manganese and Nickel oxide on Nickel foam electrodes were studied with X-ray diffractometer by varying the diffraction angles  $2\theta$  from 10 to 95 in the Fig. 1. The peaks  $44.69^\circ$ ,  $52.14^\circ$  and  $76.74^\circ$  can be indexed to the (111), (200) and (220) planes corresponding to Nickel of Nickel foam substrate (PDF #04-0850) and the shoulder peaks at  $44.75^\circ$ ,  $76.8^\circ$  can be indexed to (200) and (311) planes of NiO (PDF # 47-1049) indicating that  $\text{MnO}_2$  particles are in the amorphous phase. Owing to the easy diffusion of the electrolyte ions through electrode material making the amorphous phase of oxide materials apt for supercapacitor behaviour [28].

### 3.2 FTIR studies

The molecular vibrational spectra of MNC10, MN25, MN50, MNCA and MNCP by Fourier Transform

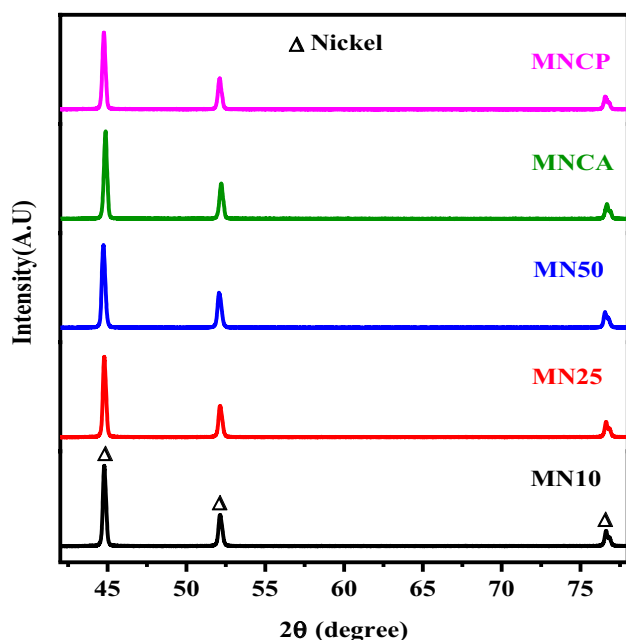


**Fig. 1** X-ray diffraction patterns of MN10, MN25, MN50, MNCA and MNCP

Infrared Spectroscopy is seen in Fig. 2. The adsorption band observed at  $540\text{ cm}^{-1}$  is ascribed to Mn–O bending mode mainly due to the distortions in  $\text{MnO}_6$  octahedra and weak band at  $461\text{ cm}^{-1}$  belong to the Ni–O stretching. The adsorption peak at  $2017\text{ cm}^{-1}$  occurs because of the degree of  $\text{H}_2$  bonding within

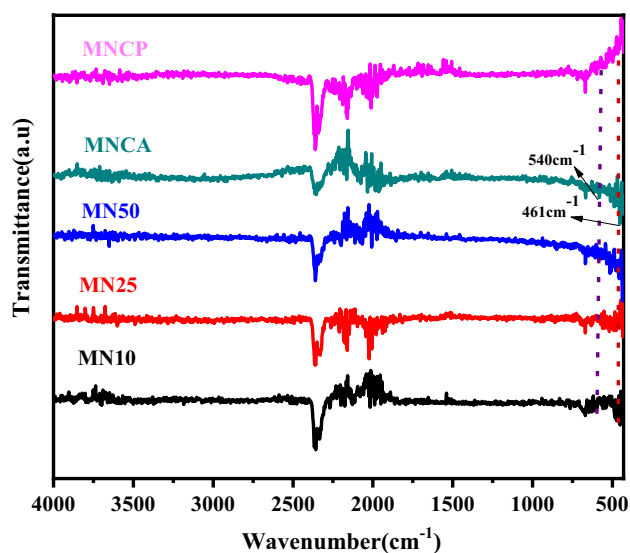


**Fig. 2** ATR-FTIR spectra of MN10, MN25, MN50, MNCA and MNCP

the electrode indicating the probable presence of the adsorbed moisture among the oxides which further enhances diffusion of ions, increasing capacitance. [39] Table 1 depicts the IR band assignments of MN10, MN25, MN50, MNCA and MNCP.

### 3.3 Surface morphological studies

The surface morphologies of the different electrodeposited electrodes were investigated by scanning electron microscopy and EDAX in Figs. 3a–e and 4a–d. Ni foam has a porous framework 3-dimensional structure and as observed from the SEM images had uniformly distributed porous structures whose roughness increased with the increase in electrodeposition cycles as well as by varying the electrodeposition method leading to densely packed  $\text{MnO}_2$  as well Nickel oxide onto the Nickel foam framework. The deposited mass load is thus increased. The possible mechanism can be attributed to the nucleation process leading to the stable linked  $\text{MnO}_2$ –NiO. This is followed by progressive nucleation, which grows on top of the already produced nuclei. Manganese and Nickel deposited electrode was observed to have a porous as well as crumbled architecture which could enhance the surface area, thereby increasing the Areal capacitance of the electrode. Table 2 gives the comparative table of elemental weight% of MN10, MN25, MN50, MNCA and MNCP. When the electrodeposition cycles are too less as well as quite high, it would affect the diffusion rate of electrolytes through the pores of the Nickel foam, thereby decreasing Areal capacitance of electrode materials.

### 3.4 Electrochemical measurements

The electrochemical performance of the electrodeposited electrodes were evaluated by cyclic voltammetry with asymmetric three electrode setup

**Table 1** IR band assignments of MN10, MN25, MN50, MNCA and MNCP

Band frequency ( $\text{cm}^{-1}$ )	Band assignment
540	Mn–O bending mode
461	Ni–O stretching
$\approx 2000$	Degree of $\text{H}_2$ bonding due to adsorbed moisture

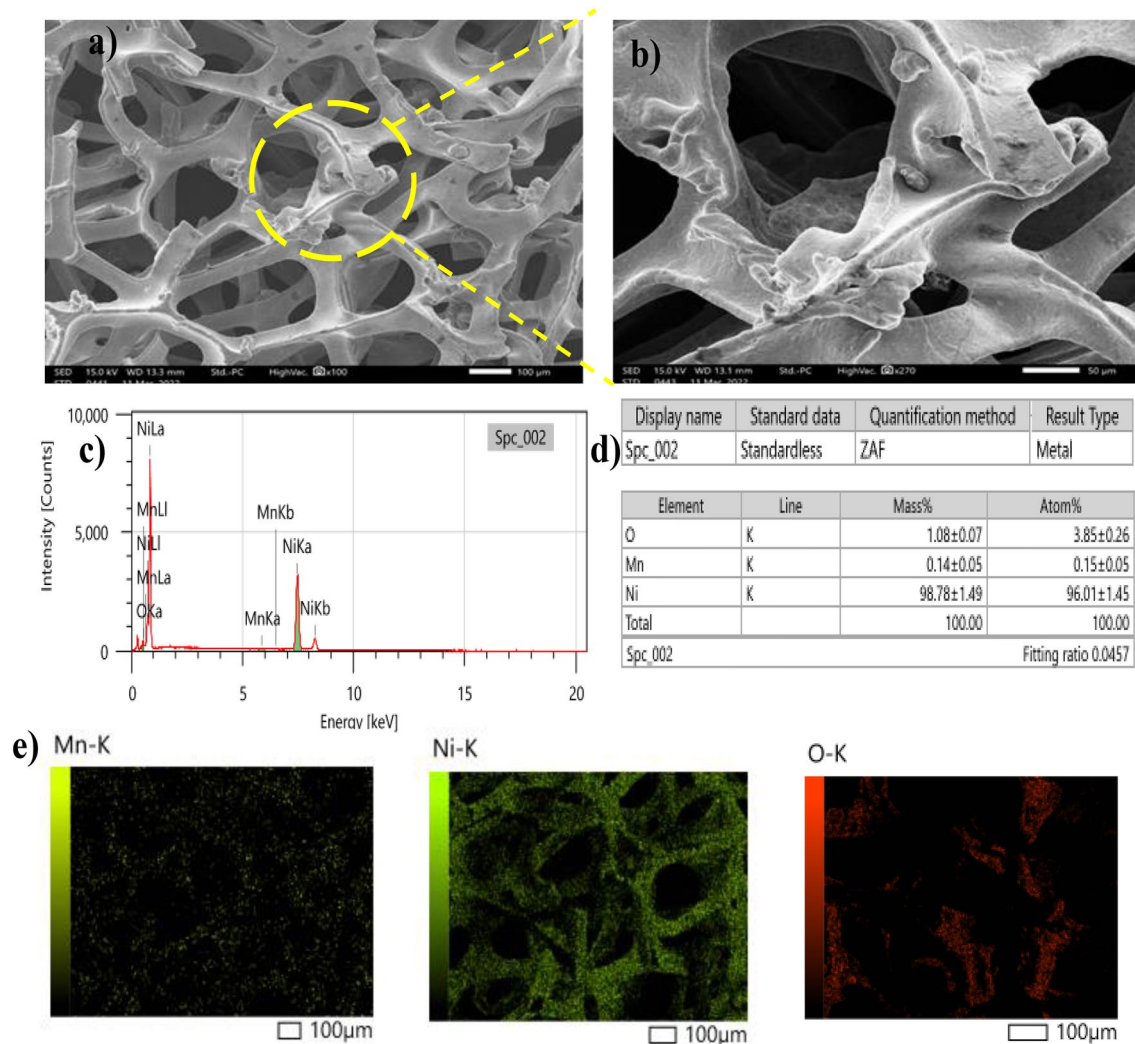


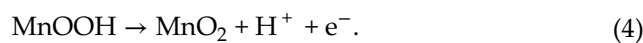
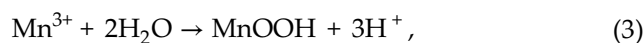
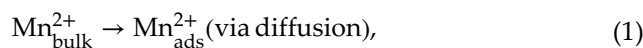
**Fig. 3** **a** Scanning electron microscopy (SEM) image of MN25, **b** enlarged area of SEM, **c** energy-dispersive spectrum, **d** comparative table of elemental weight%, **e** elemental mapping images of Mn, Ni, and O

in 0.1 M KOH electrolyte. Cyclic voltammogram Curves of the Ni foam electrodes electrodeposited with Manganese and Nickel oxides via potentiodynamic methods with varying deposition cycles; 10, 25 and 50 ( MN10, MN25, MN50), potentiostatic (MNCA) as well as galvanostatic methods (MNCP) at varying scan rates of 5, 10, 20, 50, 100 and 200 mVs<sup>-1</sup> in the voltage window of 0 to 600 mV are presented in Fig. 5.

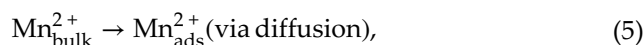
The possible electrochemical mechanism of the formation of MnO<sub>2</sub> and NiO on Nickel foam is as follows:

There are two possible electrodeposition mechanism for MnO<sub>2</sub> formation [40]:

Mechanism 1:



Mechanism 2:



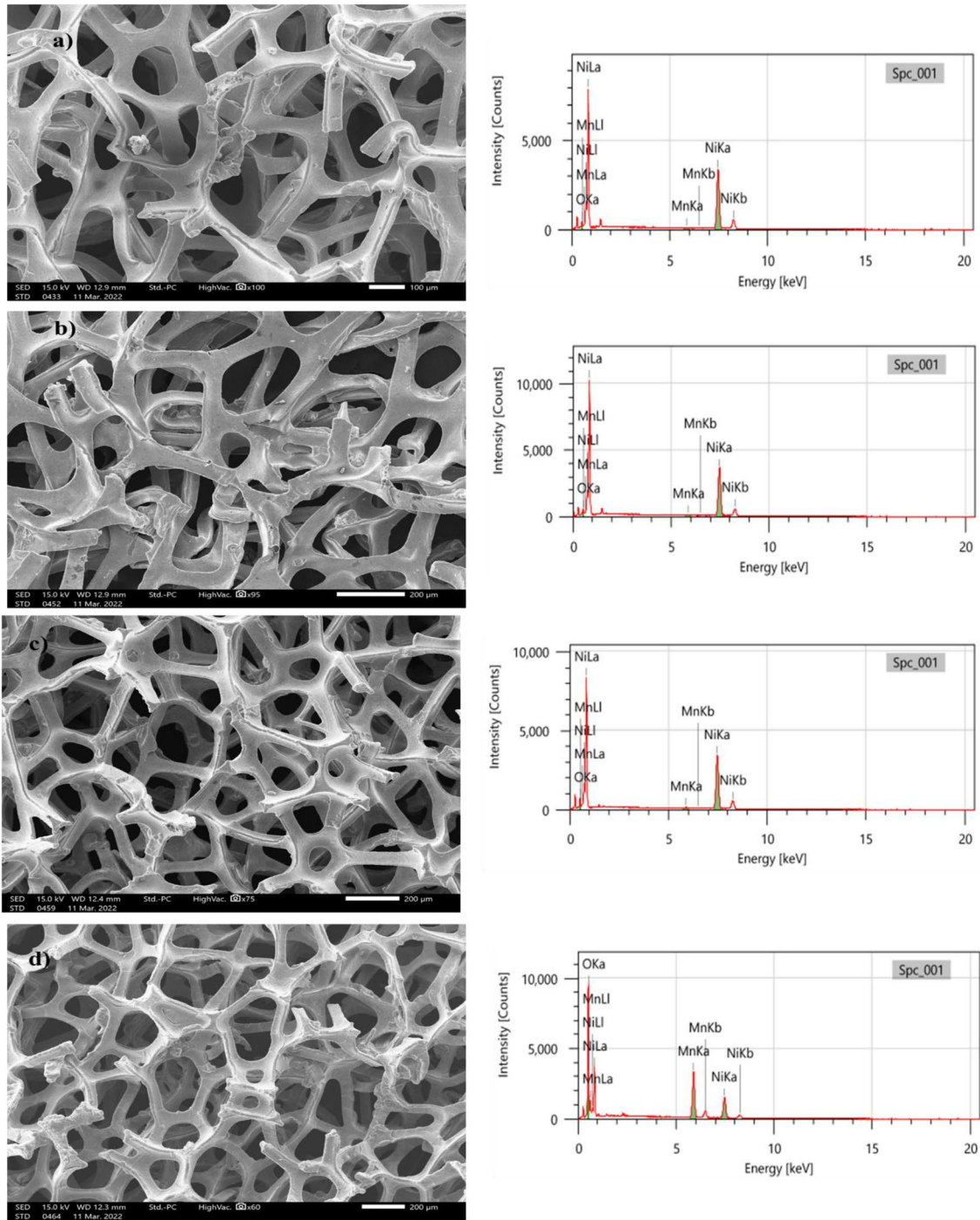
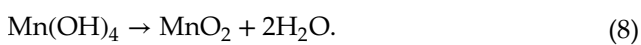
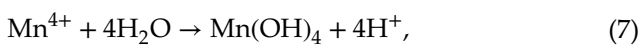


**Fig. 4** SEM image and energy-dispersive spectrum of **a** MN10, **b** MN50, **c** MNCA and **d** MNCP



NiO formation mechanism [41]:

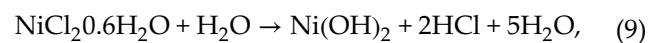


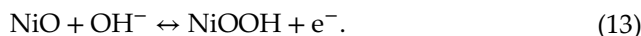
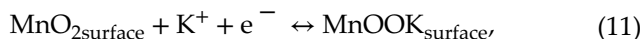
**Table 2** Comparative table of elemental weight% of MN10, MN25, MN50, MNCA and MNCP

	Mn wt%	Ni wt%	O wt%
MN10	0.04	95.57	4.39
MN25	0.14	96.01	3.85
MN50	0.24	95.32	4.43
MNCA	0.59	92.33	7.08
MNCP	23.80	21.55	54.65

The synthesised electrodes exhibited slightly different electrochemical behaviour due to the characteristics of interface of the electrode–electrolyte and the transport rate of ions to and from the surface of electrodes. It can be seen that the CV response exhibits anodic and cathodic peaks around 0.5 V and 0.4 V,

respectively, implying the occurrence of two reversible faradic processes resembling the surface redox pseudocapacitive behaviour.

The possible mechanism regarding the charge storage of both Manganese and Nickel Oxide



Equation (1) depicts the adsorption and desorption of potassium ion  $\text{K}^+$  onto the surface of  $\text{MnO}_2$  ( non-faradaic process), Eq. (2) shows the intercalation and removal of the  $\text{K}^+$  on  $\text{MnO}_2$ 's interstitial sites ( faradaic process) and Eq. (3) The capacitive behaviour of

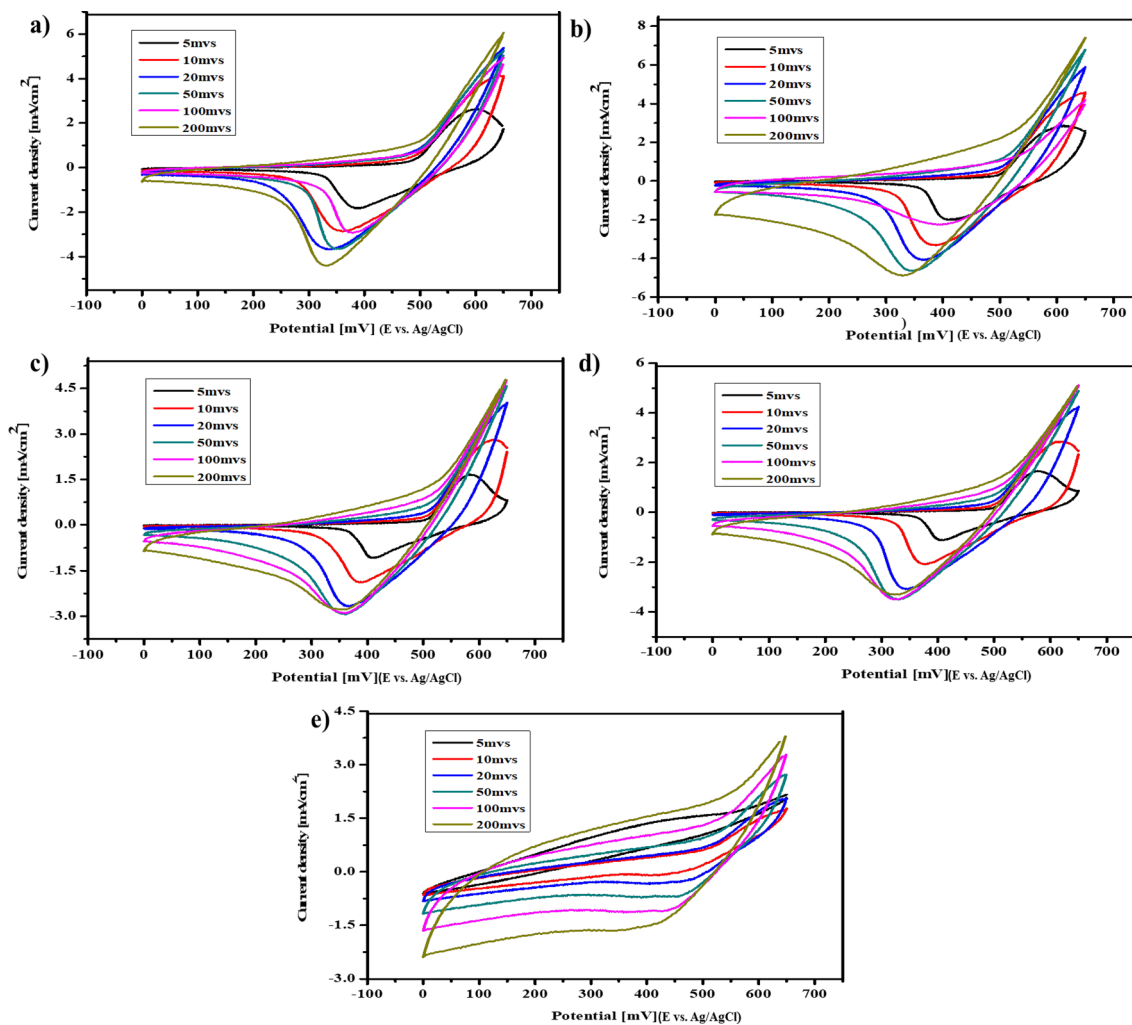


**Fig. 5** CV curves of **a** MN10, **b** MN50, **c** MNCA and **d** MNCP at varying scan rates of 5, 10, 20, 50, 100 and 200  $\text{mVs}^{-1}$

NiO in an alkaline solution is caused by the storage of charge in an electrical double layer at the electrolyte/electrode interface and redox reactions on the surface of electroactive nickel oxide and their dependency on hydroxide ion concentration. [42].

From the CV profiles versus reference electrode Ag/AgCl with increasing scan rates, the current density of all the synthesised samples also increased. However, the deviation in the CV curve shape can be attributed to lack of effective interaction between electrode and ions since there isn't enough time for the diffusions of ions into the electrode material at higher scan rates. To determine supercapacitive behaviour of the electrodes under investigation, the comparison of cyclic voltammogram of MN10, MN25, MN50, MNCA and MNCP in 0.1 M KOH at 5 mVs<sup>-1</sup> is shown in Fig. 6.

Its observed that initially the peak current density increases with increase of electrodeposition cycles, however, for electrodeposition via 50 cycles the current density decreased indicating lower diffusion rate of cations on the Manganese and nickel oxide-based electrodes because their dense and compact structure.

Equation 4 can be used to calculate the Areal capacitance (C<sub>sp</sub>) for each composite based on the CV curves

$$C_{sp} = \frac{1}{v\Delta V} \int i(V) dV. \quad (14)$$

At 5 mVs<sup>-1</sup> scan rate, the calculated Areal capacitance values of MN10, MN25, MN50, MNCA and MNCP electrodes were 179.24, 188.1, 61.24, 97.88 and 122.41 F cm<sup>-2</sup>, respectively. The better Areal

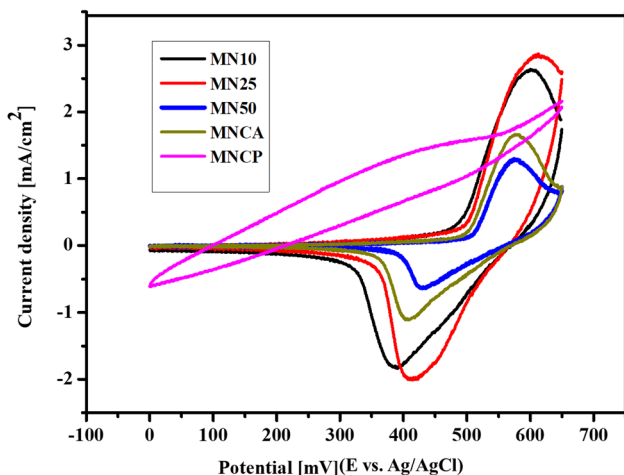


**Fig. 6** Comparison of cyclic voltammogram of MN10, MN25, MN50, MNCA and MNCP in 0.1 M KOH at 5 mVs<sup>-1</sup>

capacitance of MN25 is due to amorphousness (from XRD) and a well-distributed mesoporous structure with little agglomeration (from SEM).

GCD curves of MN10, MN25, MN50, MNCA and MNCP electrodes at varying current densities from 0.5 to 20 Acm<sup>-2</sup> versus reference electrode Ag/AgCl is observed in Fig. 7. GCD curves of all the electrodes exhibited distorted triangular shapes due to metal oxides which are pseudocapacitance materials [43, 44]. The GCD profile comprised of a resistive component resulted from a sudden voltage drop (iR drop because of the internal resistance of both MnO<sub>2</sub> and NiO), a capacitance component resulting from ions separation in the double layer region at the electrode interface, and a faradaic component resulting from MnO<sub>2</sub> charge transfer reaction in the extended time region. Comparison of charge discharge curves of MN10, MN25, MN50, MNCA and MNCP in the potential range between 0 and 600mV at a current density of 0.5 Acm<sup>-2</sup> was presented in Fig. 8. Among the different electrodeposition methods, charging and discharging time is more for the potentiodynamic electrodeposition for 10 and 25 cycles compared to potentiostatic as well as galvanostatic electrodeposition leading to higher Areal capacitance.

The Areal capacitance values were calculated from the GCD graphs using the Eq. (5).

$$C_s = \frac{I \times \Delta t}{A \times \Delta V}. \quad (15)$$

where, C<sub>s</sub>: Areal capacitance (F cm<sup>-2</sup>), I (mA): applied current density, A: area of the working electrode, Δt (s): discharging time, ΔV (V): potential window to discharge. Areal capacitance of the MN10, MN25, MN50, MNCA and MNCP are 211.33, 256.08, 73.65, 99.3 and 99.42 F cm<sup>-2</sup> at 0.5 Acm<sup>-2</sup> current density. The comparison of the Areal capacitance value from GCD curves is depicted in the bar graph in Figs. 9 and 10 depicts the areal capacitance vs. varying current densities of MN10, MN25, MN50, MNCA and MNCP.

From the Areal capacitance value, it can be seen that deposition cycle of 25 is the optimum to deposit Manganese and Nickel oxides proven by its highest Areal capacitance compared to the other electrodeposition cycles and methods. The deposited layer got thicker when deposition period on Nickel foam was increased, same was observed for both MNCA and MNCP slowing the electrolyte ions diffusion into electrode materials and lowering Areal capacitance.



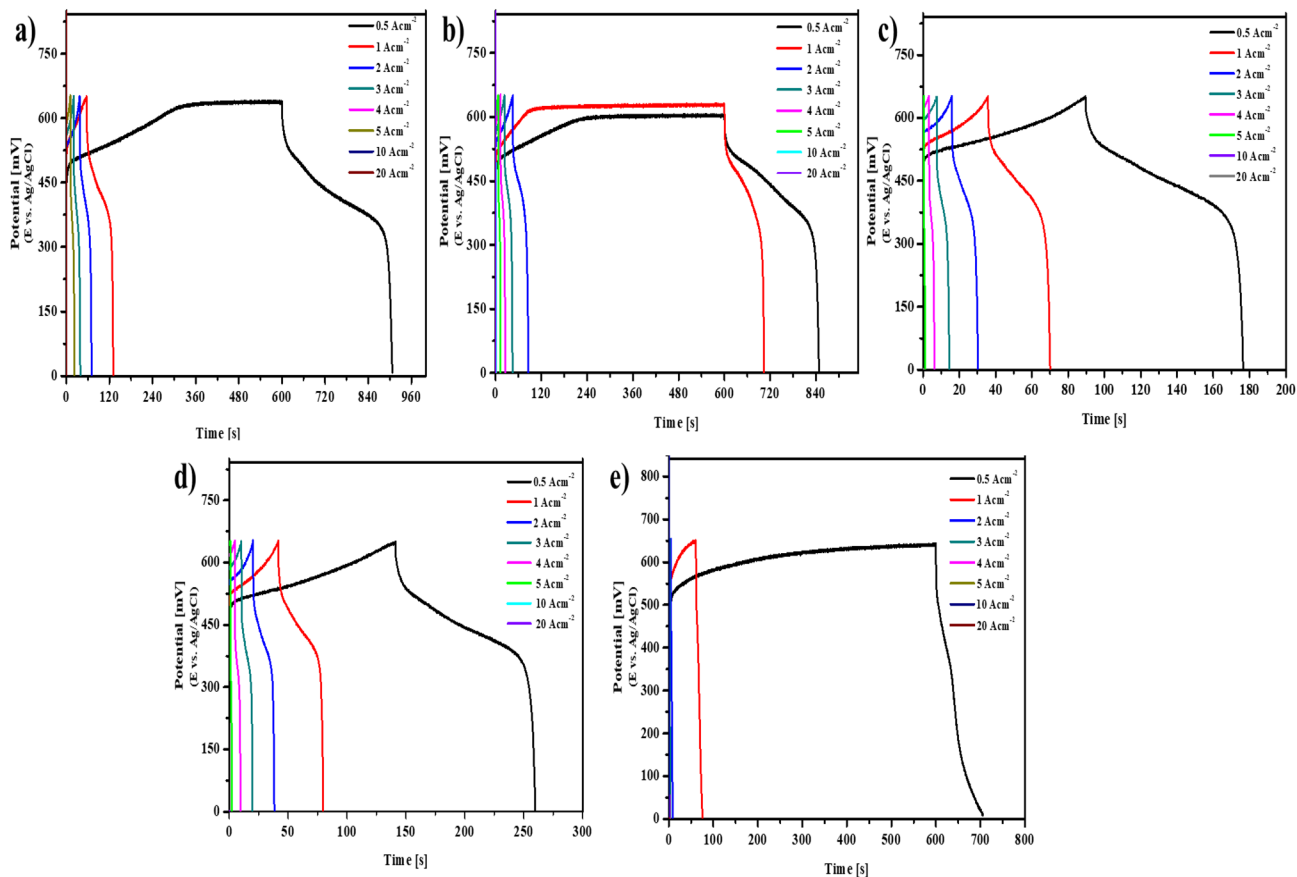


**Fig. 7** GCD curves of **a** MN10, **b** MN50, **c** MNCA and **d** MNCP at electrodes at varying current densities of 0.5, 1, 2, 3, 4, 5, 10 and 20 Acm<sup>-2</sup>

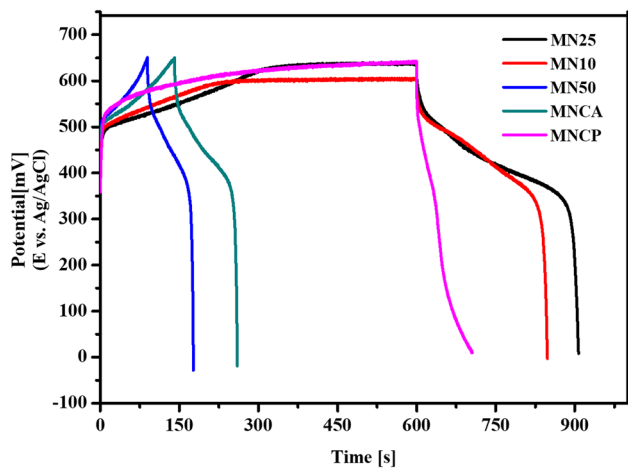


**Fig. 8** Comparison of GCD curves of MN10, MN25, MN50, MNCA and MNCP in 0.1 M KOH at current density of 0.5 Acm<sup>-2</sup>

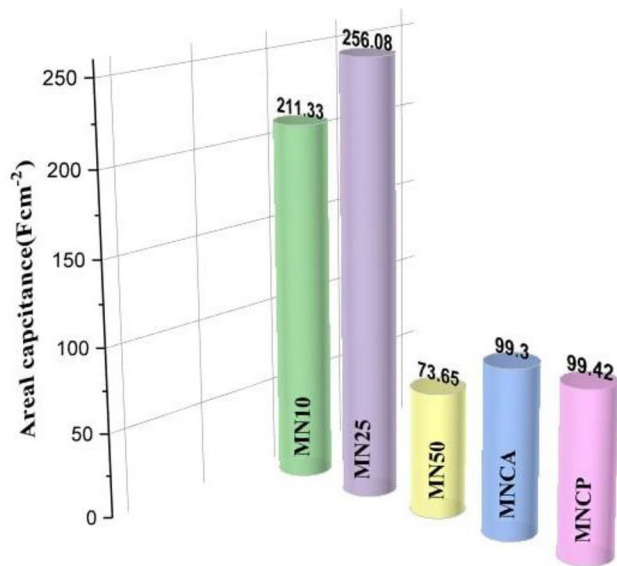


**Fig. 9** Comparison of areal capacitance value of MN10, MN25, MN50, MNCA and MNCP

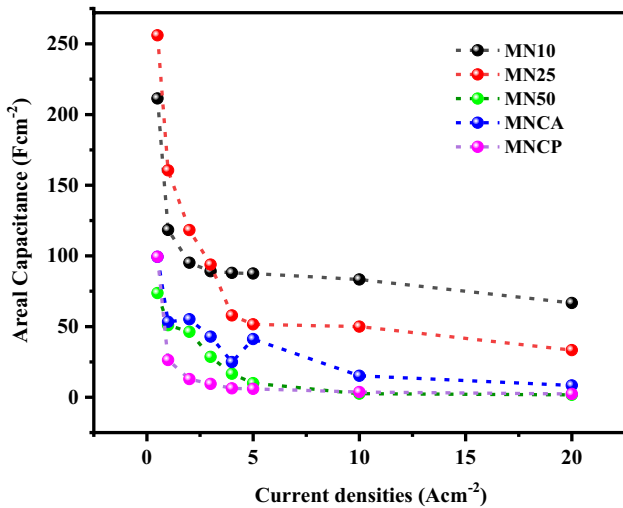


**Fig. 10** Areal capacitance vs. varying current densities (0.5 Acm<sup>-2</sup>, 1 A cm<sup>-2</sup>, 3 Acm<sup>-2</sup>, 4 Acm<sup>-2</sup>, 5 Acm<sup>-2</sup>, 10 Acm<sup>-2</sup> and 20 Acm<sup>-2</sup>) of MN10, MN25, MN50, MNCA and MNCP

To separate the capacitive properties where the capacitance and inverse of capacitance are plotted against scan rate  $v^{-1/2}$  and  $v^{1/2}$ , Trasatti method is followed [45, 46]. The data is plotted to extrapolate the capacitance value at  $i=0$  and  $v=\infty$ . Capacitance at zero mV/s showcases the total capacitance and at infinite shows the charge stored at the surface. Surface charge capacitance is studied from the plot capacitance vs.

$v^{-1/2}$ . On assuming semi-infinite linear diffusion, linear correction is expected for the plot of capacitance versus inverse square root of scan rate. In higher scan rates they deviate from linearity due to ohmic drops caused by the resistance of Manganese and Nickel oxides. The total maximum capacitance is plotted from the inverse of capacitance vs.  $v^{1/2}$ . Thus, the main aim of following the Trasatti method is to understand the capacitance contribution of EDLC and pseudocapacitance [12].

$$\frac{1}{C} = \text{constant} * v^{\frac{1}{2}} + \frac{1}{C_{\text{total}}}, \tag{16}$$

$$C = \text{constant} * v^{-\frac{1}{2}} + C_{\text{EDLC}}, \tag{17}$$

$$C_{\text{total}} = C_{\text{EDLC}} + C_{\text{PSUEDO}}. \tag{18}$$

Figure 11 (a) shows the plot of inverse of capacitance ( $C^{-1}$ ) vs. square root of scan rate ( $v^{1/2}$ ), (b) plot of capacitance vs. inverse of the square root of scan rate. We could conclude with Trasatti method, MN25, which the electrode material showing the highest capacitance among the others has 24.85% EDL capacitance and 75.15% pseudocapacitance from Fig. 11c.

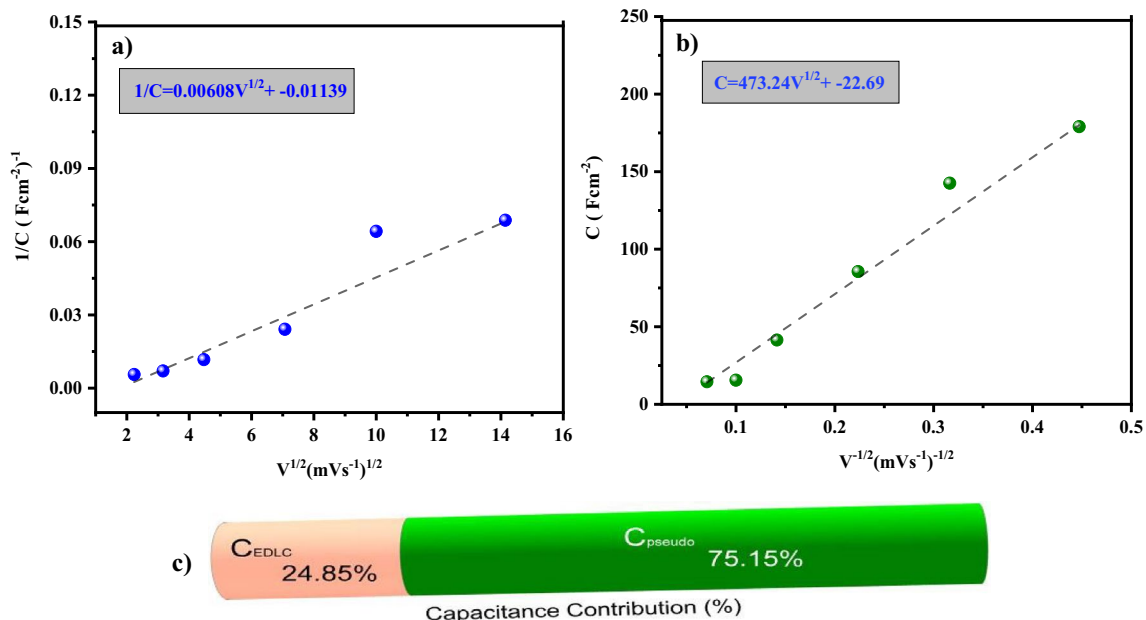


**Fig. 11** **a** Plot of inverse of capacitance ( $1/C$ ) versus the square root of scan rate ( $v^{1/2}$ ). **b** Plot of capacitance ( $C$ ) versus inverse of the square root of scan rate ( $v^{-1/2}$ ). **c** Percentage of EDL capacitance and pseudo-capacitance for MN25 by Trasatti method

The charge contribution is examined by studying the dependence of scan rate on current by Conway and Dunn's method [47, 48]. The current measured is due to the MnO<sub>2</sub> and NiO surface double layer charging as well as the pseudocapacitive current associated with faradaic reaction on the surface of Manganese ion surfaces. As the combination of these two mechanisms, one could understand the current behaviour at a particular potential.

$$i(v) = k_1v + k_2v^{\frac{1}{2}} \tag{19}$$

On dividing both sides with square root of scan rate;

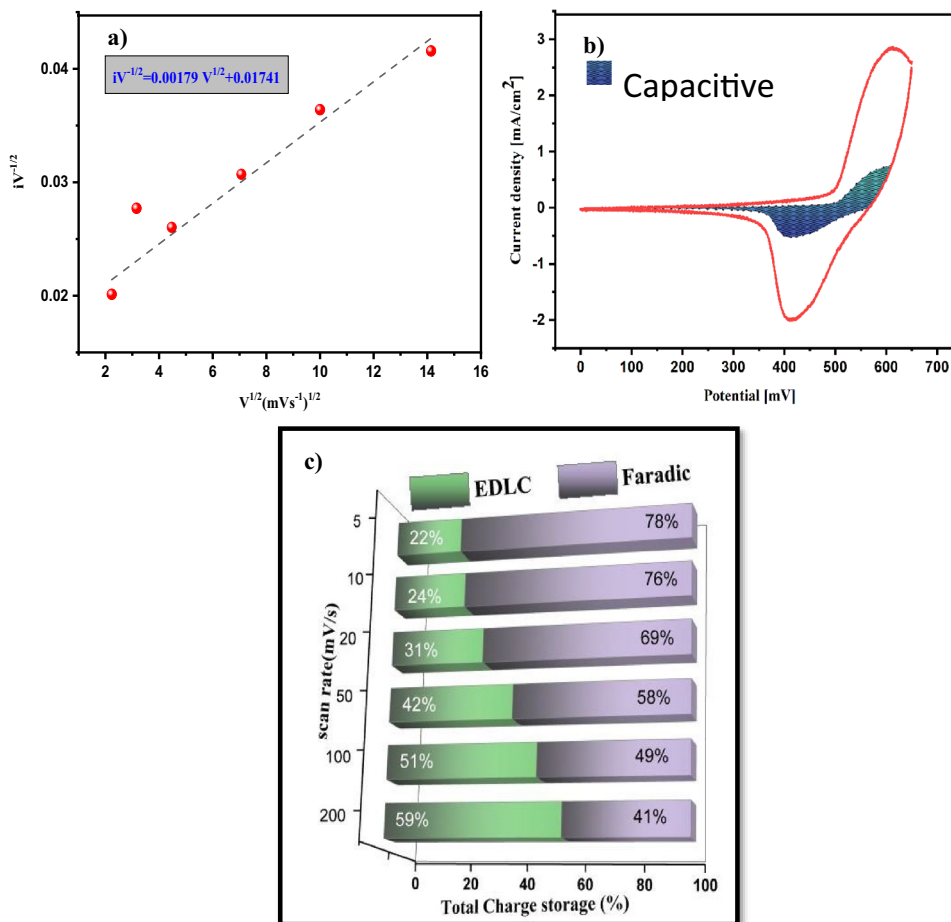
$$\frac{i(V)}{v^{\frac{1}{2}}} = k_1v^{1/2} + k_2 \tag{20}$$

where  $i(V)$  is the current response at a particular potential,  $v$  is a scan rate,  $k_1$  and  $k_2$  are scan rate-independent constant,  $k_1v$  correspond to the contribution of current from EDLC and  $k_2v^{1/2}$  corresponds to

pseudocapacitive current. Figure 12a shows the plot of  $i(V)/v^{1/2}$  vs.  $v^{1/2}$  for MN25 at the potential 0.31 V. One can determine  $k_1$  and  $k_2$  from the slope and the intercept point on the y axis due to the linear nature of the graph. Figure 12c shows the comparison of contribution by diffusion control current and capacitive current at 0.31 V for MN25 at varying scan rates. It is also observed that there is an evident change in the charge storage mechanism as we go at higher scan rates due to the fast charge and discharge process; increasing the capacitive current. On comparing the EDLC current and pseudocapacitive current, 78%, 76%, 69%, 58%, 49% and 41% of the total charge stored at scan rated 5, 10, 20, 50, 100 and 200 mVs<sup>-1</sup> belongs to faradaic current. The capacitive contribution of MN25 at 5 mVs<sup>-1</sup> is exhibited in Fig. 12b and we can confirm that the double-layer charging as well as the faradaic contribution are in accordance i.e. calculation via Dunn's method matches with the calculation via Trasatti method.

The equation  $i = av^b$  also is utilised to determine the  $b$  value which gives information about the

**Fig. 12** **a** Plot of  $i(V)/v^{1/2}$  vs.  $v^{1/2}$  of MN25 at 0.31 V. **b** Capacitive contribution of MN25 at 5 mVs<sup>-1</sup>. **c** Total charge storage contribution from EDLC and pseudocapacitance for MN25 with 0.31 V at varying scan rate



electrode material mechanism, where  $i$  is the peak current density obtained from the CV curves,  $a$  &  $b$  are adjustable parameters and  $v$  is the scan rate (mV/s).  $b$  value is derived from the slope of plot of  $\log(i)$  vs.  $\log(v)$ . The mechanism is capacitive if the value is 1 and diffusion controlled if the value is 0.5. Figure 13 showcases the plot of  $\log(i)$  vs.  $\log(v)$

(i) plot of the synthesised electrodes with the  $b$  values of MN10, MN25, MN50, MNCA and MNCP are 0.754, 0.74, 0.641, 0.712 and 0.668, respectively. indicating the charge storage mechanism involves both the diffusion and capacitive process. Table 3 gives the comparison of the  $b$  values of the electrodes with the reported literature.

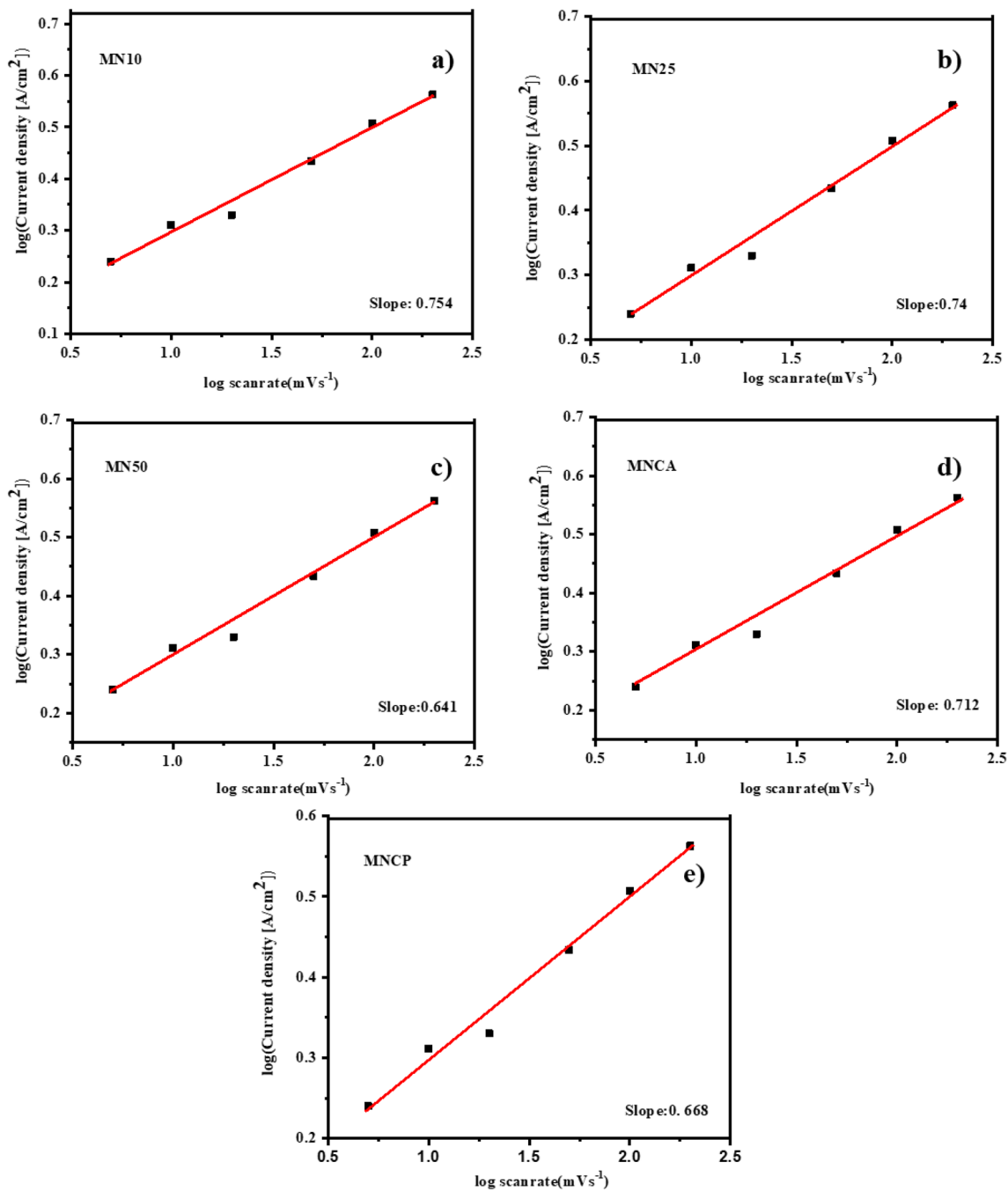


**Fig. 13** Plot of  $\log(i)$  vs.  $\log(v)$  plot of **a** MN10, **b** MN25, **c** MN50 **d** MNCA and **e** MNCP

**Table 3** Comparison of b values of synthesised electrode with reported literature

Electrode material	b value	Reference
MN10	0.754	This work
MN25	0.74	This work
MN50	0.641	This work
MNCA	0.712	This work
MNCP	0.668	This work
$\alpha$ -MnO <sub>2</sub>	0.5–0.7	[24]
MnO <sub>2</sub> -TEA	0.82	[52]
MnO <sub>2</sub> -C	0.75	[53]
NHMO-5	0.73	[54]
MnO <sub>2</sub> /CNT//AC	0.63	[55]

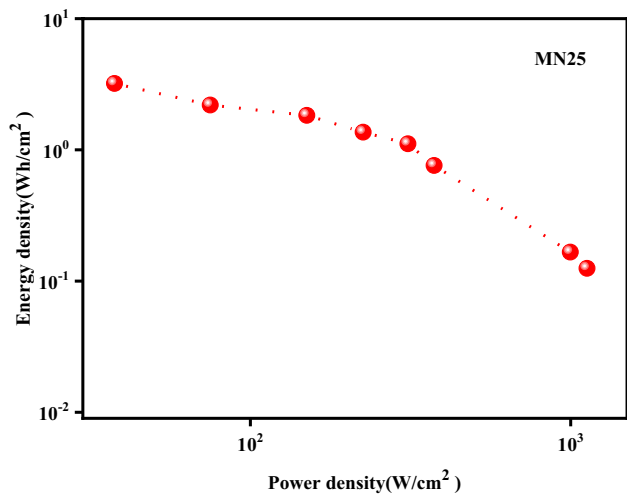


**Fig. 14** Ragone plot of MN25 electrode

The energy density (Wh/cm<sup>3</sup>) and power density  $P$  (W/cm<sup>3</sup>) of the electrodeposited electrodes are obtained from the two electrode system based on Eqs. (21) and (22)

$$E = \frac{0.5 * C * \Delta V^2 * 1000}{3600}, \tag{21}$$

**Table 4** Comparison of Areal capacitance from CV and GCD, Energy density and Power density of the electrodeposited electrodes

	Areal capacitance [CV] (F cm <sup>-2</sup> )	Areal capacitance [GCD] (F cm <sup>-2</sup> )	Energy density (Wh/cm <sup>3</sup> )	Power density (W/cm <sup>3</sup> )
MN10	179.24	211.33	2.52	35.75
MN25	188.1	256.08	3.05	35.88
MN50	61.24	73.65	0.88	35.69
MNCA	97.88	99.3	0.28	35.59
MNCP	122.41	99.42	4.97	35.71

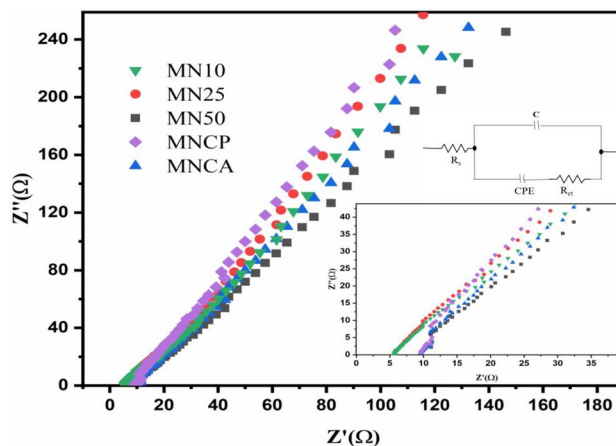


**Fig. 15** Nyquist plots for MN10, MN25, MN50, MNCA and MNCP in 0.1 M KOH; inset of enlarged Nyquist plot and equivalent circuit of MN25

$$P = \frac{E * 3600}{\Delta t}, \tag{22}$$

where  $C$  : Areal capacitance,  $\Delta V$  (V): potential window, and the  $\Delta t$  (s) : discharge time. It is observed that highest power density of 35.88 Wcm<sup>-3</sup> was observed at the energy density range of 3.05 Whcm<sup>-3</sup> for MN25 at charging rate 0.5 Acm<sup>-2</sup> among other electrodes.

Ragone plot of MN25 at the charging rate 0.5, 1, 2, 3, 4, 5, 10 and 20 Acm<sup>-2</sup> is displayed in Fig. 14. Table 4 shows the comparison of the Areal capacitance value, energy and power density of the electrodeposited electrode materials.

EIS studies in the frequency range of 100 kHz to 1 mHz are used to explore the electrochemical characteristics of the electrode/electrolyte interface. The Nyquist plots for MN10, MN25, MN50, MNCA and MNCP in 0.1 M KOH are observed in Fig. 15. Corresponding electrical circuit of MN25 was created by fitting the impedance data. The interfacial charge transfer resistance ( $R_{ct}$ ) occurs at the interface between the electrode and the electrolyte due to the electrical charge transfer in the redox process of the electrode

materials. The total of electrode materials' intrinsic resistance, the electrolyte's ionic resistance and the contact resistance at the electrode material and current collector interface is the internal resistance ( $R_s$ ). To account for capacitance, constant phase element was applied. Based on the fitted EIS results, the values of  $R_s$  of MN10, MN25, MN50, MNCA and MNCP are calculated to be 5.669  $\Omega$ , 5.52  $\Omega$ , 9.71  $\Omega$ , 9.87  $\Omega$  and 11.07  $\Omega$  and  $R_{ct}$  values are 1.78  $\Omega$ , 0.2  $\Omega$ , 1.2  $\Omega$ , 0.117  $\Omega$  and 3.03  $\Omega$  respectively. From the Nyquist plot, the charge-transfer resistances of MN25 is the least revealing the improved ion and charge transfer along with the conductivities of the electrode material.

Among the synthesised electrode, since MN25 exhibited higher Areal capacitance; the stability was assessed by Galvanostatic Charge Discharge curves (GCD). Capacitance retention plot of MN25 at current density of 5  $\text{Acm}^{-2}$  before and after 5000 cycles shows 80.5% of discharge time was retained even at 5000th cycle as seen in Fig. 16. From literatures, it is proposed that the decrease in capacitive retention with cycling is caused by the partial dissolution

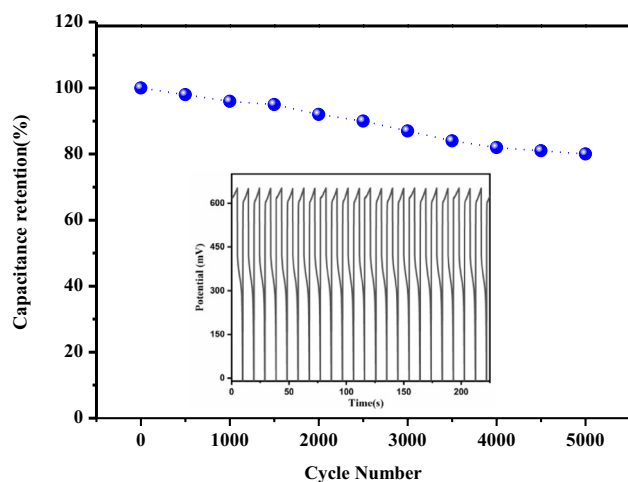


**Fig. 16** Cyclic stability of MN25

of manganese oxide to formation of soluble  $\text{Mn}^{2+}$ . Another possible reason is due to the active materials' gradual detachment from Nickel foam due to the continuously increasing number of cycles leading to reduced specific capacitance [49–51]. Table 5 displays the comparison of areal capacitance of different metal oxides w.r.t. MN25.

## 4 Conclusion

Manganese and Nickel oxides were successfully deposited onto Nickel foam substrate via different electrodeposition. The scanning electron microscopy images along with EDX indicated how the morphology and deposition is affected due to potentiodynamic, potentiostatic and galvanostatic methods. XRD pattern exhibited significant peaks of Nickel foam with shoulder peaks belonging to NiO indicated the amorphous phase of  $\text{MnO}_2$ . Variations in the electrochemical behaviour was revealed in the cyclic voltammograms, GCD curves with the change in the mode of electrodeposition. Among them, electrodeposition potentiodynamically for 25 cycles (MN25) showcased higher areal capacitance 256.08  $\text{F cm}^{-2}$ , energy density 12.81  $\text{Wh cm}^{-3}$  and power density 150.71  $\text{W cm}^{-3}$  compared to MN10, MN50, MNCA and MNCP. MN25 also showed cyclic stability of 5000 cycles with 80.5% of capacitance retention percentage at 5  $\text{Acm}^{-2}$ . Charge transfer resistance was also observed to be relatively lower for MN25 compared to other electrodes thus having better conductivity, ionic transfer thus behaving as an apt supercapacitor electrode material.

**Table 5** Comparison of areal capacitance of different metal oxides w.r.t. MN25

Different metal oxides/combinations	Current ( $\text{mA/cm}^{-2}$ )	Synthesis method	Areal capacitance	Reference
$\text{MnO}_2/\text{MoS}_2$	0.1	Magnetron sputtering	224 $\text{mF cm}^{-2}$	[56]
$\text{NiCo}_2\text{O}_4$	0.133	Sol-gel method	40.6 $\text{mF cm}^{-2}$	[57]
$\text{NiCo}_2\text{O}_4/\text{MnO}_2$	1	Hydrothermal	5.3 $\text{Fcm}^{-2}$	[58]
$\text{ZnCo}_2\text{O}_4/\text{Ni(OH)}_2$	2	Electrochemical deposition	4.6 $\text{Fcm}^{-2}$	[59]
MN25	0.5	Electrodeposition	256.08 $\text{F cm}^{-2}$	Present work

## Acknowledgements

Authors are grateful to the Researchers Supporting Project Number (RSP2023R326), King Saud University, Riyadh, Saudi Arabia. Also, the authors would like to thank the basic research support from the National Institute of Technology Puducherry, Karaikal, India.

## Author contributions

AR performed the investigation, MC contributed to data interpretation, MRS and SMW project administration, and funding acquisition, ME contributed to the writing of the original draft and RD contributed to writing, reviewing, and editing the manuscript.

## Funding

This work was supported by King Saud University (Grant No: RSP2023R326).

## Data availability

The data that support the findings of this study are available from the corresponding author, upon reasonable request.

## Declarations

**Conflict of interest** The authors report no declaration of interest.

## References

1. M. Hoel, S. Kverndokk, *Res. Energy Econ.* **18**, 115 (1996). [https://doi.org/10.1016/0928-7655\(96\)00005-X](https://doi.org/10.1016/0928-7655(96)00005-X)
2. T.N. Veziroğlu, S. Şahi, *Energy Convers. Manag.* **49**, 1820 (2008). <https://doi.org/10.1016/j.enconman.2007.08.015>
3. M. Höök, X. Tang, *Energy Policy.* **52**, 797 (2013). <https://doi.org/10.1016/j.enpol.2012.10.046>
4. A. Raveendran, M. Chandran, S.M. Wabaidur, M.A. Islam, R. Dhanusuraman, VK Ponnusamy, *Fuel.* **324**, 124424 (2022). <https://doi.org/10.1016/j.fuel.2022.124424>
5. M. Chandran, A. Raveendran, A. Thomas, M. Vinoba, S.K. Jeong, M. Bhagiyalakshmi, *Synth. Met.* **293**, 117260 (2023). <https://doi.org/10.1016/j.synthmet.2022.117260>
6. J.B. Goodenough, H.D. Abruna, M.V. Buchanan, Basic research needs for electrical energy storage. Report of the basic energy sciences workshop on electrical energy storage, 2–4 April 2007. <https://doi.org/10.2172/935429>
7. J.W. Duay, Electrochemical Synthesis, transformation, and characterization of MnO<sub>2</sub> nanowire arrays for supercapacitor electrodes (2013). <http://hdl.handle.net/1903/14499>
8. R. Dhanusuraman, P. Chahal, A. Raveendran et al., *J. Energy Storage.* **60**, 106554 (2023). <https://doi.org/10.1016/j.est.2022.106554>
9. X. Lin, M. Salari, L.M.R. Arava, P.M. Ajayan, M.W. Grinstaff, *Chem. Soc. Rev.* **45**, 5848 (2016). <https://doi.org/10.1039/C6CS00012F>
10. PN Pintauro, *Polym. Rev.* **55**, 201 (2015). <https://doi.org/10.1080/15583724.2015.1031378>
11. M. Chandran, I. Shamna, A. Anusha, M. Bhagiyalakshmi, *SN Appl. Sci.* (2019). <https://doi.org/10.1007/s42452-019-0509-1>
12. M. Chandran, A. Thomas, A. Raveendran, M. Vinoba, M. Bhagiyalakshmi, *J. Energy Storage.* **30**, 101446 (2020). <https://doi.org/10.1016/j.est.2020.101446>
13. Z. Wu, Y. Zhu, X. Ji, C.E. Banks, *Nanomater. Adv. Batteries Supercapacitors* (2016). [https://doi.org/10.1007/978-3-319-26082-2\\_9](https://doi.org/10.1007/978-3-319-26082-2_9)
14. B. De, S. Banerjee, K.D. Verma, T. Pal, P. Manna, K.K. Kar, *Handbook of Nanocomposite Supercapacitor Materials II: Performance* (Springer, Berlin, 2020). [https://doi.org/10.1007/978-3-030-52359-6\\_4](https://doi.org/10.1007/978-3-030-52359-6_4)
15. M. Muthuselvi, K. Jeyasubramanian, G. Hikku et al., *Int. J. Energy Res.* **45**, 8255 (2021). <https://doi.org/10.1002/er.6441>
16. W.H. Low, P.S. Khiew, S.S. Lim, C.W. Siong, E.R. Ezeigwe, *J. Alloys Compd.* **775**, 1324 (2019). <https://doi.org/10.1016/j.jallcom.2018.10.102>
17. D. Lincot, *Thin Solid Films.* **487**, 40 (2005). <https://doi.org/10.1016/j.tsf.2005.01.032>
18. W. Schwarzacher, *Electrochem. Soc. Interface.* **15**, 32 (2006). <https://doi.org/10.1149/2.F08061IF>
19. G.A. Ali, M.M. Yusoff, Y.H. Ng, H.N. Lim, K.F. Chong, *Curr. Appl. Phys.* **15**, 1143 (2015). <https://doi.org/10.1016/j.cap.2015.06.022>
20. H.Y. Lee, J.B. Goodenough, *J. Solid State Chem.* **144**, 220 (1999). <https://doi.org/10.1006/jssc.1998.8128>
21. S. Devaraj, N. Munichandraiah, *Electrochem. Solid-State Lett.* **8**, A373 (2005). <https://doi.org/10.1149/1.1922869>

22. D. Dubal, D. Dhawale, T. Gujar, C. Lokhande, *Appl. Surf. Sci.* **257**, 3378 (2011). <https://doi.org/10.1016/j.apsusc.2010.11.028>
23. E. Muthusankar, D. Ragupathy, *Mater. Lett.* **241**, 144 (2019). <https://doi.org/10.1016/j.matlet.2019.01.071>
24. M. Jayachandran, A. Rose, T. Maiyalagan, N. Poongodi, T. Vijayakumar, *Electrochim. Acta.* **366**, 137412 (2021). <https://doi.org/10.1016/j.electacta.2020.137412>
25. L. Hu, W. Chen, X. Xie et al., *ACS nano.* **5**, 8904 (2011). <https://doi.org/10.1021/nn203085j>
26. P. Tang, Y. Zhao, C. Xu, *Electrochim. Acta.* **89**, 300 (2013). <https://doi.org/10.1016/j.electacta.2012.11.034>
27. M. Arvani, J. Keskinen, D. Lupo, M. Honkanen, *J. Energy Storage.* **29**, 101384 (2020). <https://doi.org/10.1016/j.est.2020.101384>
28. T. Gujar, V. Shinde, C. Lokhande, W.-Y. Kim, K.-D. Jung, O.-S. Joo, *Electrochem. Commun.* **9**, 504 (2007). <https://doi.org/10.1016/j.elecom.2006.10.017>
29. S. Rahimi, S. Shahrokhian, H. Hosseini, *J. Electroanal. Chem.* **810**, 78 (2018). <https://doi.org/10.1016/j.jelechem.2018.01.004>
30. V. Kovalenko, V. Kotok, I. Kovalenko, (2018) Восточно-Европейский журнал передовых технологий, 56
31. N.A. Salleh, S. Kheawhom, A.A. Mohamad, *Arab. J. Chem.* **13**, 6838 (2020). <https://doi.org/10.1016/j.arabjc.2020.06.036>
32. X. Zhang, X. Wang, L. Jiang, H. Wu, C. Wu, J. Su, *J. Power Sources.* **216**, 290 (2012). <https://doi.org/10.1016/j.jpowsour.2012.05.090>
33. C. Zhong, Y. Deng, W. Hu, J. Qiao, L. Zhang, *J. Zhang, Chem. Soc. Rev.* **44**, 7484 (2015). <https://doi.org/10.1039/C5CS00303B>
34. M.J. Carmezim, C.F. Santos, *Metal Oxides Supercapacitors.* (2017). <https://doi.org/10.1016/B978-0-12-810464-4.00003-6>
35. J. Yin, J. Park, *Microporous Mesoporous Mater.* **200**, 61 (2014). <https://doi.org/10.1016/j.micromeso.2014.08.016>
36. L. Gu, Y. Wang, R. Lu, L. Guan, X. Peng, J. Sha, *J. Mater. Chem. A* **2**, 7161 (2014). <https://doi.org/10.1039/C4TA00205A>
37. M. Chandran, A. Raveendran, M. Vinoba, B.K. Vijayan, M. Bhagiyalakshmi, *Ceram. Int.* **47**, 26847 (2021). <https://doi.org/10.1016/j.ceramint.2021.06.093>
38. H. Jeong, L.K. Kwac, C.G. Hong, H.G. Kim, *Mater. Sci. Eng.: C* **118**, 111510 (2021). <https://doi.org/10.1016/j.msec.2020.111510>
39. M Mylarappa, VV Lakshmi, KV Mahesh, H Nagaswarupa, N Raghavendra (2016) IOP Conference series: materials science and engineering, IOP Publishing, <https://doi.org/10.1016/j.matpr.2017.09.152>
40. C.J. Clarke, G.J. Browning, S.W. Donne, *Electrochim. Acta.* **51**, 5773 (2006). <https://doi.org/10.1016/j.electacta.2006.03.013>
41. A. Sonavane, A. Inamdar, P. Shinde, H. Deshmukh, R. Patil, P. Patil, *J. Alloys Compd.* **489**, 667 (2010). <https://doi.org/10.1016/j.jallcom.2009.09.146>
42. D.T. Dam, X. Wang, J.-M. Lee, *Nano Energy.* **2**, 1303 (2013). <https://doi.org/10.1016/j.nanoen.2013.06.011>
43. A. Huang, M.F. El-Kady, X. Chang et al., *Adv. Energy Mater.* **11**, 2100768 (2021). <https://doi.org/10.1002/aenm.202100768>
44. K. Allado, M. Liu, A. Jayapalan, D. Arvapalli, K. Nowlin, *Energy Fuels* **35**, 8396 (2021). <https://doi.org/10.1021/acs.energyfuels.1c00556>
45. S. Ardizzone, G. Fregonara, S. Trasatti, *Electrochim. Acta.* **35**, 263 (1990). [https://doi.org/10.1016/0013-4686\(90\)85068-X](https://doi.org/10.1016/0013-4686(90)85068-X)
46. J. Duay, S.A. Sherrill, Z. Gui, E. Gillette, S.B. Lee, *Acs Nano.* **7**, 1200 (2013). <https://doi.org/10.1021/acs.energyfuels.1c00556>
47. J. Wang, J. Polleux, J. Lim, B. Dunn, *J. Phys. Chem. C* **111**, 14925 (2007). <https://doi.org/10.1021/jp074464w>
48. K. Brezesinski, J. Wang, J. Haetge et al., *J. Am. Chem. Soc.* **132**, 6982 (2010). <https://doi.org/10.1021/ja9106385>
49. R. Gummow, A. De Kock, M. Thackeray, *Solid State Ionics.* **69**, 59 (1994). [https://doi.org/10.1016/0167-2738\(94\)90450-2](https://doi.org/10.1016/0167-2738(94)90450-2)
50. S. Sivakkumar, J.M. Ko, D.Y. Kim, B. Kim, *Electrochim. Acta* **52**, 7377 (2007). <https://doi.org/10.1016/j.electacta.2007.06.023>
51. S. Singhal, A. Shukla, *J. Solid State Electrochem.* **24**, 1271 (2020). <https://doi.org/10.1007/s10008-020-04615-0>
52. A. Zhang, R. Zhao, L. Hu, et al., *Adv. Energy Mater.* **11**, 2101412 (2021). <https://doi.org/10.1002/aenm.202101412>
53. A. Zhang, R. Gao, L. Hu, et al., *Chem. Eng. J.* **417**, 129186 (2021). <https://doi.org/10.1016/j.cej.2021.129186>
54. H. Duan, Z. Zhao, J. Lu et al., *ACS Appl. Mater. Interfaces.* **13**, 33083 (2021). <https://doi.org/10.1021/acsami.1c08161>
55. X. Tan, S. Liu, Q. Guo et al., *Int. J. Energy Res.* **44**, 4556 (2020). <https://doi.org/10.1002/er.5235>
56. H. Zhang, J. Wei, Y. Yan, et al., *J. Power Sources.* **450**, 227616 (2020). <https://doi.org/10.1016/j.jpowsour.2019.227616>
57. Y. Liu, N. Wang, C. Yang, W. Hu, *Ceram. Int.* **42**, 11411 (2016). <https://doi.org/10.1016/j.ceramint.2016.04.071>
58. L. Su, L. Gao, Q. Du et al., *J. Alloys Compd.* **749**, 900 (2018). <https://doi.org/10.1016/j.jallcom.2018.03.353>
59. Y. Pan, H. Gao, M. Zhang, L. Li, G. Wang, X. Shan, *J. Colloid Interface Sci.* **497**, 50 (2017). <https://doi.org/10.1016/j.jcis.2017.02.053>



**Publisher's Note** Springer nature remains neutral with regard to jurisdictional claims in published maps and institutional affiliations.

Springer Nature or its licensor (e.g. a society or other partner) holds exclusive rights to this article under a publishing

agreement with the author(s) or other rightsholder(s); author self-archiving of the accepted manuscript version of this article is solely governed by the terms of such publishing agreement and applicable law.